Simultaneous Imaging and Spectroscopy of the EUV Sun: First Flight of *MOSES*

Charles C. Kankelborg
Department of Physics
Montana State University

September 4, 2006

Contents

1 Introduction

We have demonstrated a new type of imaging spectrograph for observing the EUV solar atmosphere. The *Multi-Order Solar EUV Spectrograph* (*MOSES*) sounding rocket payload was launched from White Sands Missile Range February 8, 2006. High resolution images of the solar atmosphere at $\lambda 304\,\text{Å}$ were obtained with line profile information over a 20×10 arc minute field of view (§ 6).

MOSES is the first instrument to provide *simultaneous* imaging and spectroscopy of dynamic events in EUV. A preliminary analysis of the data is given in § 7.1, showing two strong downflow events in the transition region, and one explosive event. In two of the three analyzed events, evidence is found for a two component line profile.

Much has been learned about the theory of this new instrument type (§ A). Based on these theoretical underpinnings, inversion techniques have been developed and tested to support future in-depth analysis of the rocket data (§ 7.2).

In addition to the technical results which are the primary focus of this report, the project has had considerable educational impact (§ B).

2 Instrument Concept

The *MOSES* concept, illustrated in figure 1, was first described by Kankelborg, Longcope, & Martens (2000) and by Kankelborg & Thomas (2001). The instrument is a slitless, objective grating spectrograph. By taking images at three spectral orders $m = -1, 0, +1$, it is possible to acquire spatial and spectral information simultaneously over a wide field of view (FOV). The passband is limited to a few spectral lines by multilayer coatings so that the data inversion for spectral information is tractable. In principle, detectors may be placed at any number of spectral orders. If more orders are recorded, more spectral information will be obtained.

The theory of the instrument is worked out in the Appendix, § A. A first analysis of the rocket data in § 7.1 validates the concept of simultaneous imaging spectroscopy with *MOSES*. What we have learned so far about more advanced analysis techniques is presented in § 7.2.

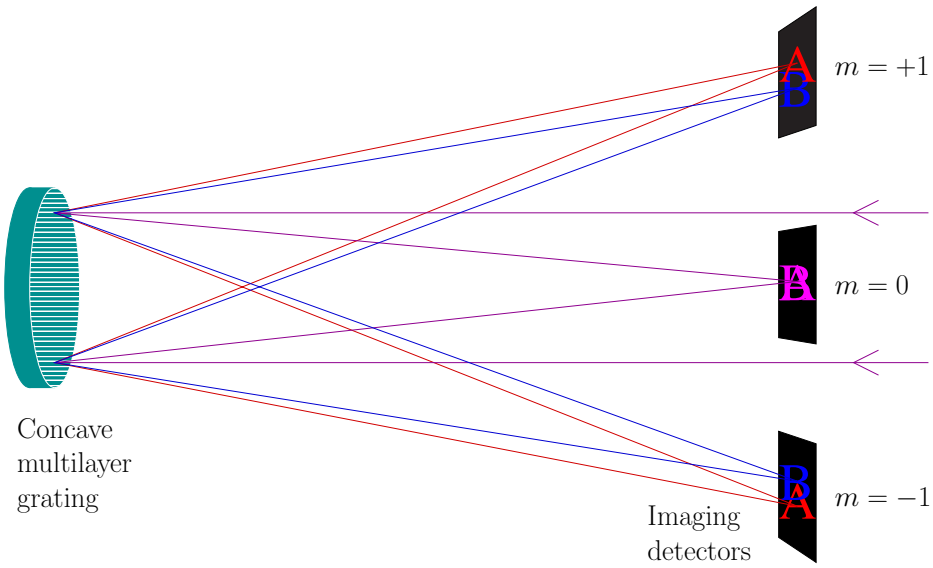

Figure 1: Conceptual sketch of *MOSES*.

3 Payload Design

3.1 Optics

The optical configuration of *MOSES* is illustrated schematically in figure 2. Instrument optical design parameters are summarized in table 1. The design was ray traced and optimized by Roger Thomas at Goddard Space Flight Center (GSFC) (Thomas & Kankelborg 2001). The major optical elements are shown in figure 3. Thin film aluminum filters (not shown) cover the open end of each detector housing to make a light tight box.

The grating flown on *MOSES* was a Zerodur substrate with spherical figure and laminar rulings fabricated by Carl Zeiss Laser Optics. Precise control of the groove depth allows an optimal the distribution of light in the three central spectral orders, where our detectors are placed. The fold flat is ULE with a protected aluminum coating on the reverse side for instrument alignment. Multilayer coatings were applied to the gratings and fold flat at GSFC.

Robust kinematic mounts for the primary (grating) and secondary (fold flat) mirror mounts were patterned after mounts manufactured for the LM-

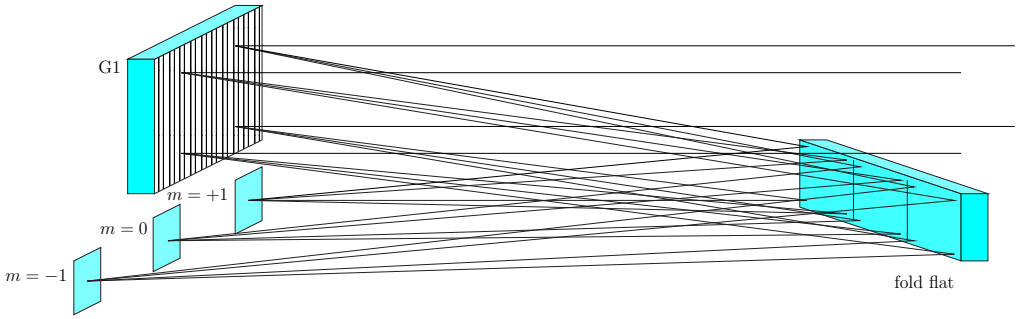

Figure 2: Sketch of the *MOSES* optical layout. Incident radiation from the right is imaged by an off-axis concave grating G1 onto detectors at three spectral orders $m = -1, 0, +1$. The optical path is folded by a flat mirror.

Table 1: Optical Characteristics

Focal length	4.74 m
Aperture	8 cm square $(f/59)$
Pixel subtent	$0\farcs59$, 29 mÅ, 29 km/s
FOV	$20' \times 10'$
Grating	9.48 m sphere, 950 lines/mm
Coatings	B_4C/Mg_2Si multilayer,
	Reflectivity ~ 0.4 ,
	$\lambda 304$ Å
Filters	1500 Å Al on Ni mesh,
	38 mm diameter
	1 each at $m = \pm 1$, 2 at $m = 0$.
Lines	He II 303.8 Å, Si XI 303.3 Å

SAL *Solar Plasma Diagnostics Experiment* (*SPDE*). Precision hemispherical pads locate the front surface (3) and sides (2+1) of each mirror, with spring loaded set screws opposing each hemisphere along a straight load path through the mirror. The set screws are inserted almost to maximum spring deflection, leaving approximately 0.001 in. of travel on the spring. If the mirror position or orientation is shifted during vibration, the springs return it immediately to alignment. The mount design makes it possible to remove

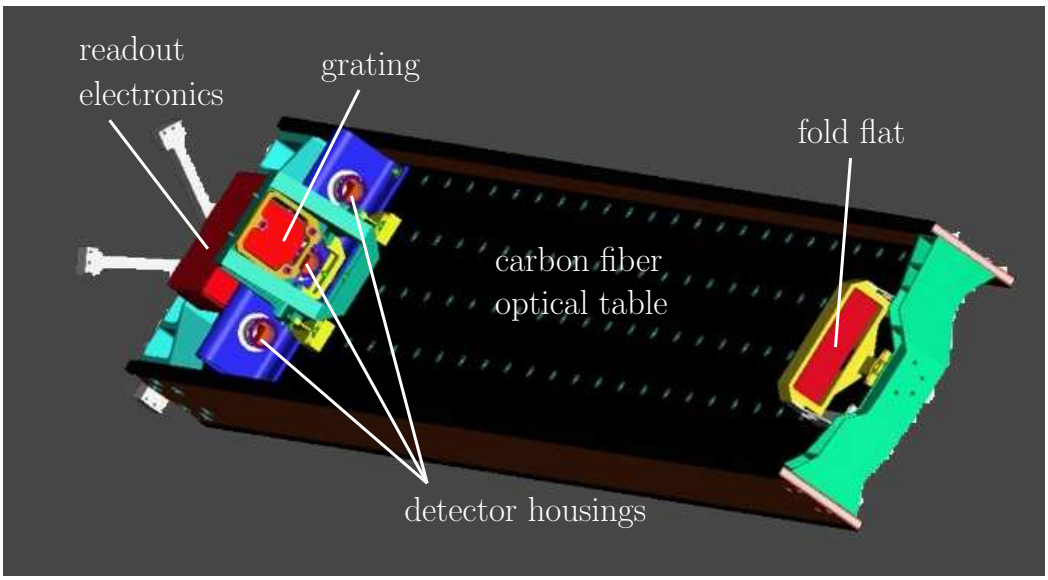

Figure 3: Layout of the *MOSES* instrument. Not shown are the baffles, front aperture plate, shutter and LN2 plumbing. Most of the payload electronics and the H-alpha video imager are on the opposite side of the optical table.

the grating and replace it with a grating ruled for work in visible light, without changing the alignment. This arrangement was very helpful for optical integration and testing.

3.2 Detectors

The detectors are three 2048×1024, rear-illuminated E2V CCD42-20 devices at spectral orders $m = -1, 0, +1$. The readout electronics is a three-channel variant of the *Solar-B*/EIS system, contributed by Mullard Space Science Laboratory (MSSL). The power supply is also a copy of the corresponding EIS system. Thermoelectric coolers (figure 4) regulate CCD temperature. An aluminum block, kept cold with liquid nitrogen (LN2) until launch, is the heat dump for the thermal control system.

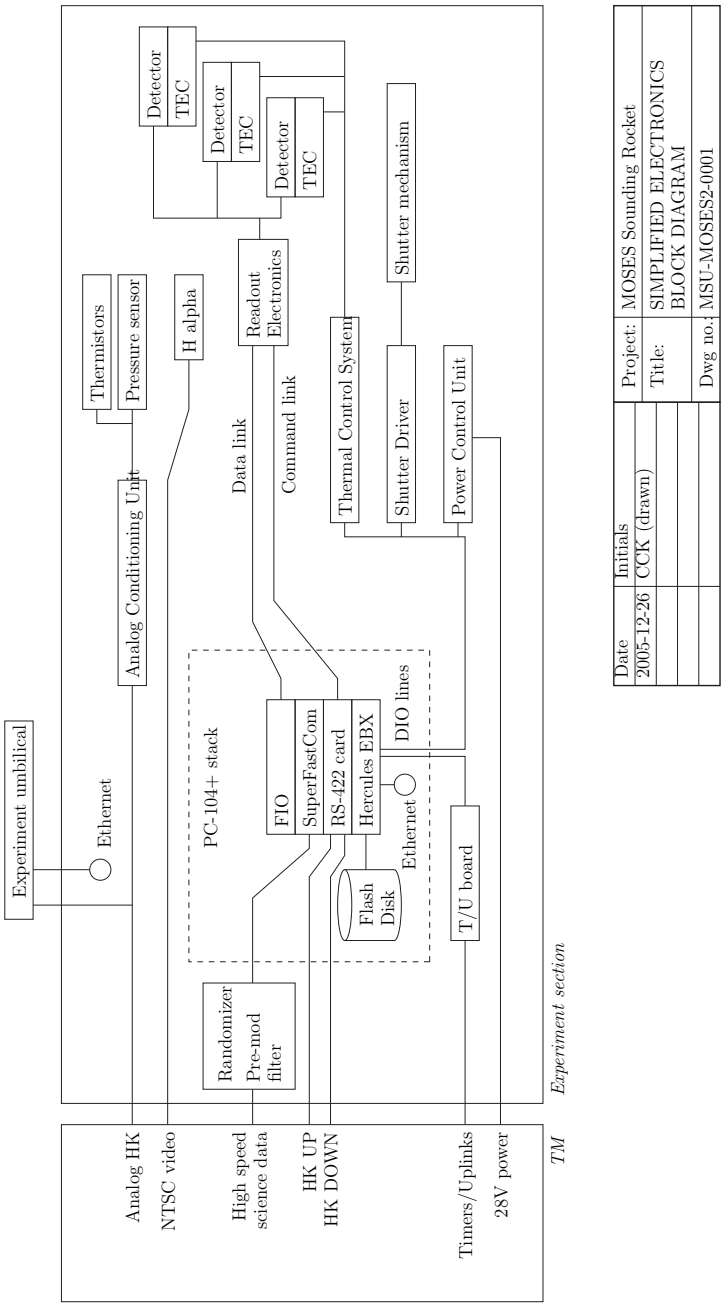

Figure 4: *MOSES* electronics system.

3.3 Electronics

A simplified block diagram of the *MOSES* electronics is shown in figure 4. Data handling and experiment control is through a single experiment computer, a Diamond Systems Hercules EBX CPU board running a minimal Linux distribution. A PC/104+ stack on the CPU board contains COTS cards for serial communications, camera data interface, and high speed telemetry. Heat from the motherboard and other stack elements are removed via heat pipes to a manifold that is linked to the heat dump LN2 line. Figure 5 shows the PC/104+ stack. .

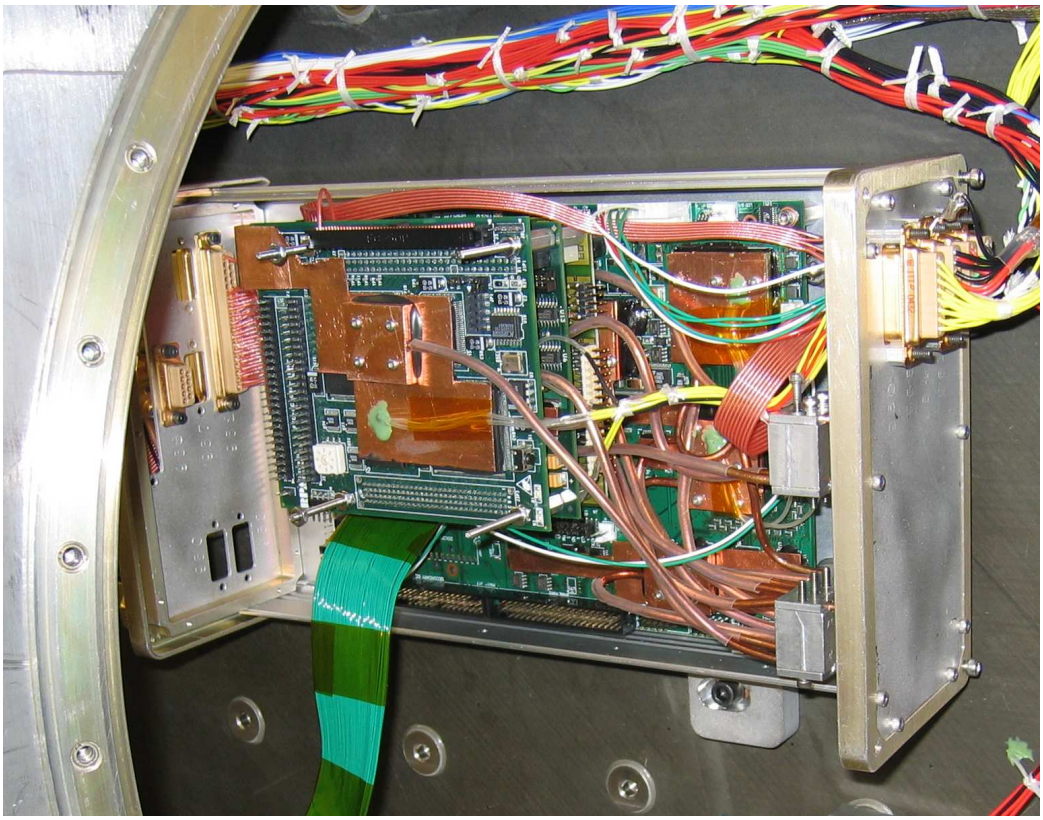

Figure 5: The *MOSES* PC/104+ stack. Heat pipes (thick copper tubes) run from the components with greatest power dissipation to the manifold at right.

All science data is stored onboard in a 1 GB flash disk. As much science

data as possible is sent to high speed telemetry during flight. Serial uplink and downlink channels allow two-way communication with the experiment computer, including a stream of detailed housekeeping data that is displayed on the *MOSES* EGSE. Standard ASCL uplinks are available to the computer through the DIO interface that is integral to the CPU board. The DIO interface also controls subsystem power and the shutter.

Custom circuits were designed, built and tested at MSU for power control, randomization and filtering of the high speed telemetry stream, CCD temperature control, pressure monitoring, timer/uplink interface, conditioning of analog data, and driving the shutter mechanism.

4 Calibration

A thorough EUV calibration of *MOSES* was undertaken in three stages:

1. CCD flat field measurements obtained at Goddard Space Flight Center.
2. BNL and NIST measurements of the MOSES gratings and multilayers.
3. End-to-end calibration of the instrument at Rutherford Appleton Laboratory.

The following sections expand on the specific motivation and results of each calibration measurement.

4.1 Flat Fields

The spectroscopic measurement to be made by *MOSES* is sensitive to differences between, and small-scale variations within, the three images obtained simultaneously at $m = -1, 0, 1$. Consequently, flat fielding of the three spectral orders is especially important.

MOSES has an unvignetted optical design. The range of field angles subtended by the detectors is too small to show any response variation due to the multilayer rocking curve. Consequently, the only response variation over the field of view is due to the CCD detectors.

A flat fielding experiment was undertaken by Lewis Fox, Roger Thomas and Marvin Schwartz at GSFC in April, 2004.

The EUV hollow cathode source does not provide uniform illumination: it contains large-scale variations due to the geometry of the hollow cathode

and the aperture, as well as small-scale variations due to the filter mesh. Our best measurements of the beam profile are the flat field images themselves, taken at a series of overlapping positions within the beam. The flat field and beam profile are derived by an iterative fitting procedure. Sample results are shown in figures 6, 7 and 8.

Figure 6: Flat field image for detector 1 ($m = -1$).

Analysis of flat field data for the detectors used at orders $m = -1$ and $m = 0$ shows a very flat response (figure 6). The flat fields correspond well with the lists of dark pixels provided by MSSL when the CCDs were procured. They also show subtle details associated with the CCD manufacturing process (figure 7). The corresponding EUV beam estimates demonstrate recovery of the faint shadow of the filter mesh (figure 8). The flat field software needs revision to improve its handling of signal statistics, and in its present state does not work for the $m = 1$ detector. We will return to the analysis this fall, and final flat fields for all three detectors are expected to be available soon.

4.2 Component Measurements

Reflectivity measurements for the *MOSES* fold flat and gratings were made at NIST's SURF III and Brookhaven's X24C beamlines, respectively (Owens

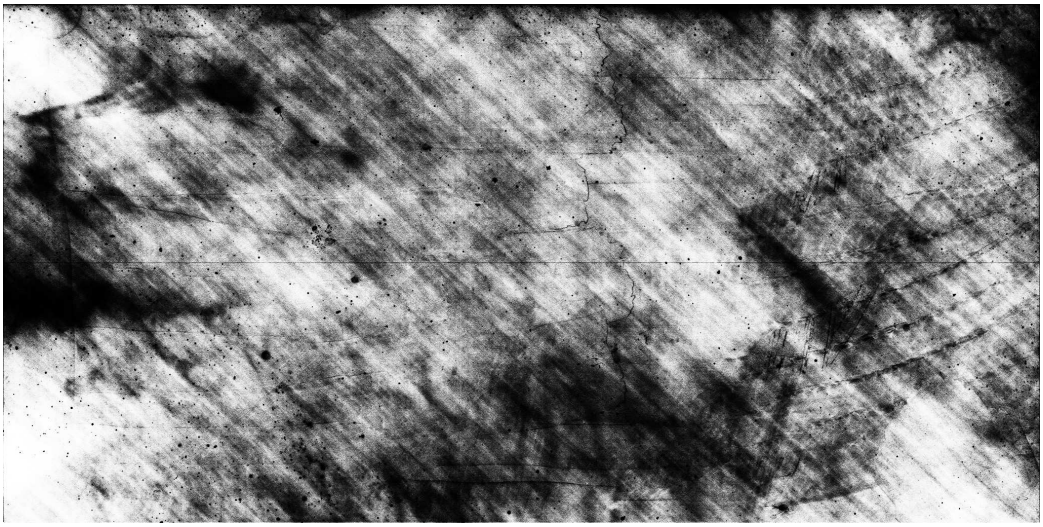

Figure 7: Flat field image for detector 1 ($m = -1$). The image has been histogram equalized to bring out subtle details.

Figure 8: Beam image derived from the detector 1 flat field data. Since images were taken at several positions, the recovered beam image is wider than the detector.

et al. 2005). These measurements demonstrate the high throughput (nearly 40%) and strong out-of-band suppression of the B_4C/Mg_2Si multilayer coatings. The coatings also passed standard pull tests and showed little change after annealing for 6 hours at 100° C. To our knowledge, *MOSES* is the first space mission to use this new multilayer, which shows great promise for future applications.

Owens et al. (2005) found that, allowing for multilayer efficiency, the grating groove efficiency is very close to the optimum specification of 50% at $m = 0$ and 25% at $m = \pm 1$. Diffraction into higher orders is strongly suppressed.

4.3 Measurements at RAL

A secondary goal of the rocket mission is calibration of *SOHO*/CDS. The *MOSES* instrument, as configured for the 2006 flight, was calibrated end-to-end at Rutherford Appleton Laboratory (RAL) in Spring 2005. The photometric accuracy of this calibration relies on the well-characterized PTB hollow cathode source, which has been calibrated by direct comparison the BESSY synchrotron. The effort of RAL was supported by the CDS investigation.

A first analysis of the RAL calibration data was completed by Thomas (2006). The response to He II λ303.8 Å radiation is 0.0084 DN per incident photon in $m = \pm 1$, 0.0042 in $m = 0$.

5 Optical Testing

The *MOSES* gratings and flat mirrors were tested individually by the manufacturers to meet specification, and subsequently at GSFC by Maria Nowak to verify compliance. The measurements made included wavefront error, radius of curvature, groove spacing (via placement of the spectral orders), and AFM measurements of groove depth and profile. All delivered components met or exceeded (and often far exceeded) their design specifications.

5.1 Instrument Focus

The primary mirror (grating) has an f-ratio of about 60 and a radius greater than 9 m. Measuring this large radius proved challenging. For grating G1

which was flown, five trials at GSFC (Nowak 2004) gave an average radius of 9482.5 mm, with a standard deviation of 1.2 mm and a spread of 3.2 mm among the measurements. The EUV depth of field for the instrument is 0.8 mm. Similar difficulty was encountered at MSU in locating the best instrument focus. Our first efforts used a Foucault test. More consistent results were obtained by autocollimation.

In the most successful version of the focus experiment, a large aperture, high quality Newtonian telescope was autocollimated using a retroreflector and a green He/Ne laser. The laser illuminated a 25 μm spatial filter in a $\sim$ 5 : 1 eyepiece projection. The Newtonian precision focuser was equipped with a micrometer dial gauge for repeatable adjustments. Retroreflected light was returned through a beam splitter behind the spatial filter to a photodiode. Best focus (maximum return signal) was determined by curve fitting. Then the collimated beam was used to form an image in the *MOSES* central order. This was done for a series of positions of the Newtonian precision focuser, the best focus being found by fitting the curve of spot size vs. focal position. The focus correction for *MOSES* was then determined by a straightforward optical calculation. The outboard orders cannot be tested independently for focus because the grating dispersion is set for EUV; for the outboard orders, we rely on the symmetry of the grating and measure the detectors into place with reference to the central order.

Because of the slow beam of the *MOSES* system, the focus procedure depends on fitting curves for very shallow extrema. The improvement of our techniques for focus determination will be a priority for future flights. We also intend to set up the grating in a Wadsworth mount to diagnose any curvature of the ruling pattern that might lead to asymmetric focal lengths in the outboard orders.

6 Flight 36.193

MOSES was launched successfully on a Terrier Black Brant sounding rocket from White Sands Missile Range on 2006 Feb 8 at 18:44 UT. Live video from the onboard Hα imager confirmed nominal pointing. Apogee was close to the nominal 260 km. All science data was recovered from the intact payload. Backup science data was received via high speed telemetry.

The exposure sequence for the February 8 flight was well chosen thanks to the end-to-end calibration at Rutherford Appleton Laboratory (§ 4.3).

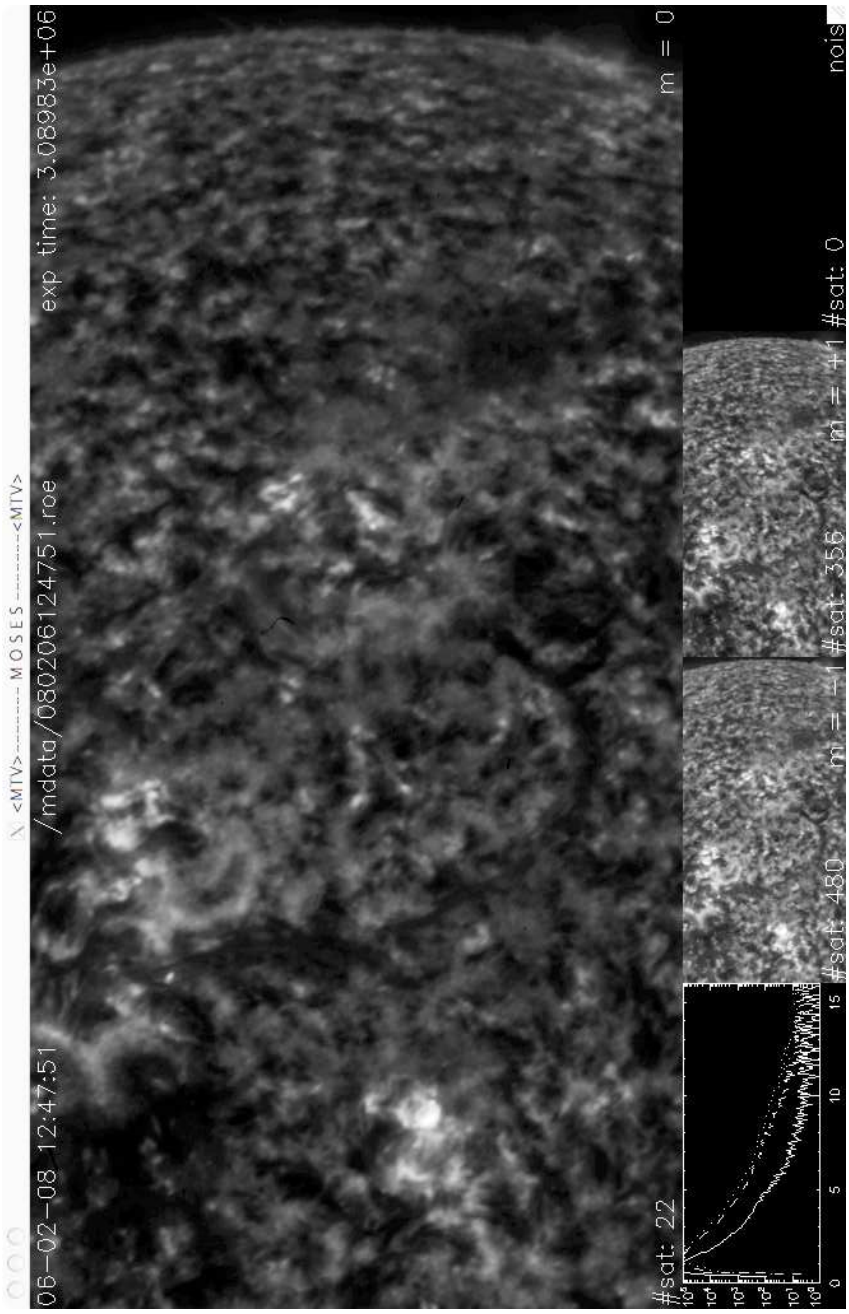

Figure 9: A sample 3 s exposure, showing all three spectral orders, from the 2006-Feb-09 *MOSES* flight. the grayscale has been altered to compress the dynamic range; it is otherwise unprocessed.

Twenty-seven science exposures, ranging from 0.25-24 s, were obtained above our nominal observing threshold of 160 km altitude. Because of the variation in atmospheric opacity, the range of *effective* exposure times is approximately 0.13-24 s.

Most of the 5 minute sequence consists of a well-exposed, rapid cadence movie of 3 second exposures. An example 3 s exposure is displayed in figure 9, which shows the central order image with insets of the outboard orders. Image resolution and dynamic range are outstanding: the J-shaped filament near the center of the image shows multiple resolved dark strands, yet the brightest element of the emerging active region (near the bottom of the figure) has barely saturated. Dark images at operating temperature were obtained before flight and during ascent.

Coordinated observations were carried out by *TRACE*, *SoHO* CDS, EIT, and several ground-based instruments. The *MOSES* launch window was timed to coincide with best *TRACE* observing during eclipse season.

7 Analysis

The following outline summarizes the *MOSES* data analysis plan.

1. Reduction (§ 7.1)
   (a) Dark subtraction, flat fields
   (b) *Coregistration* of $m = -1, 0, +1$ to 0.2 pixel (6 km/s)
   (c) Removal of drift
2. Scientific analysis
   (a) Preliminary analysis (§ 7.1)
      i. Spectral signatures in *difference* between orders
      ii. Centroid features; "parallax" ⇒ doppler shift
   (b) Inversions (§ 7.2)
      i. Compensate for *PSF*, different in each order
      ii. Inversion algorithms—apply globally or locally

The next two sections present a preliminary analysis and describe the capabilities we have developed for inversion of the data.

7.1 Data reduction and preliminary analysis

Figure 9 shows a minimally processed *MOSES* image. After dark subtraction and removal of flat fields, the images from the three spectral orders must be aligned as accurately as possible. All spectral measurements depend on this step. We use a low-order polynomial coordinate transformation for coregistration, allowing for the slight distortion that is present in the outboard ($m = \pm 1$) images:

$$x' = \sum_{i=0}^{1} \sum_{j=0}^{1} a_{ij} x^i y^j, \tag{1}$$

$$y' = \sum_{i=0}^{1} \sum_{j=0}^{1} b_{ij} x^i y^j. \tag{2}$$

The images were deemed aligned when the sum of the square of the residuals, normalized by intensity (in the manner of χ^2_R) was minimized as a function of the polynomial warping coefficients a_{ij} and b_{ij}.[1] By aligning the three orders, we effectively assume a zero mean doppler shift over the FOV; the measurement of nonzero mean doppler shift would require calibration of the instrument with an extremely well-collimated EUV line source, which was not available to us. The alignments of the three spectral orders were repeatable from exposure to exposure, to better than 0.2 pixel RMS. No measurable relative movement of the detectors should occur in flight, so the median alignment across all of the 3 s exposures was taken as the alignment for the entire sequence.

In a difference image, say $I_+ - I_0$, we expect doppler shifts to show up as black-and-white bipolar features because of dispersion. We will now briefly summarize the properties of three observed events that show strong spectral signatures in $I_+ - I_0$. These features are identified in figure 10.

The three panels of figure 11 show Feature 1 in I_+, I_0, and $I_+ - I_0$. The bipole in the third panel indicates a strong redshift. Over time, an extended bipolar lobe of the same sense grows out of the bottom of this feature. By comparing the centroids of the feature in I_+ and I_0 (figure 12), it is possible to derive an average doppler shift of 36 km/s. The dispersed order shows a bimodal shape. Evidently, there are two distinct components: a strong redshift and a weaker blueshift.

[1] In this application, the most consistent results are found when χ^2_R is normalized by the number of *overlapping* pixels, which is itself a function of the alignment parameters.

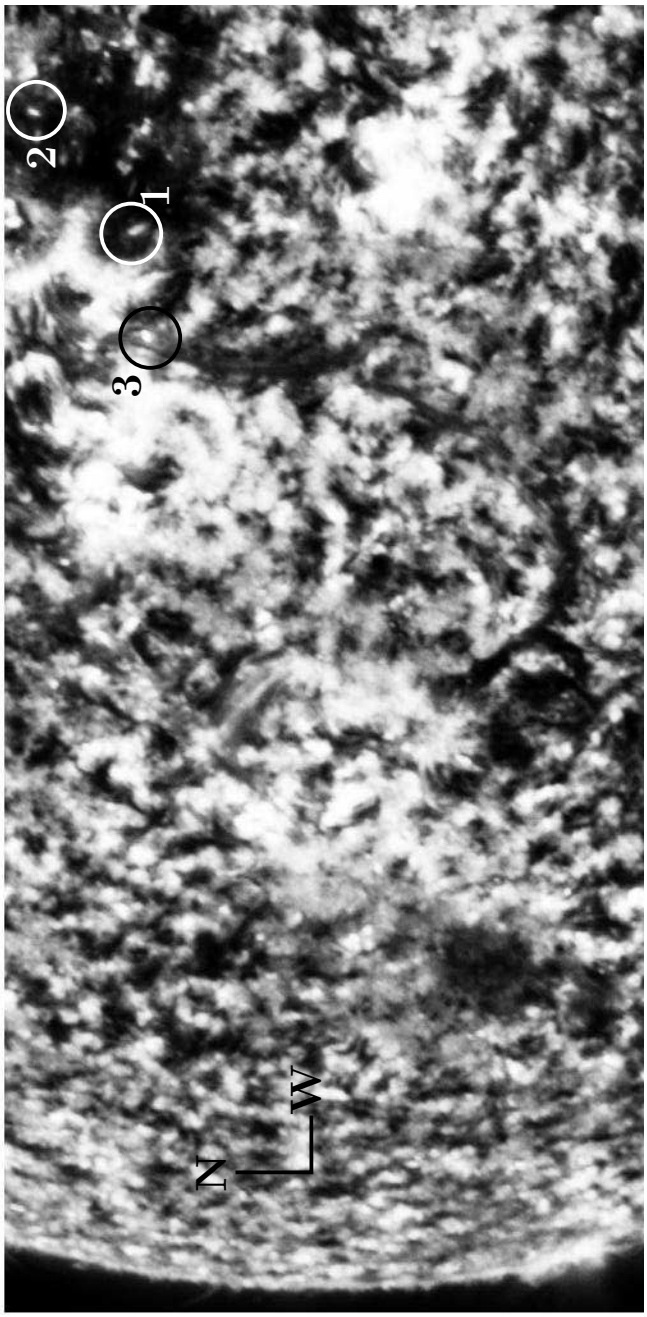

Figure 10: Location of features analyzed in this section. Exposure 19 of 27, $m = 0$, 3 s. The image is histogram equalized to bring out faint details.

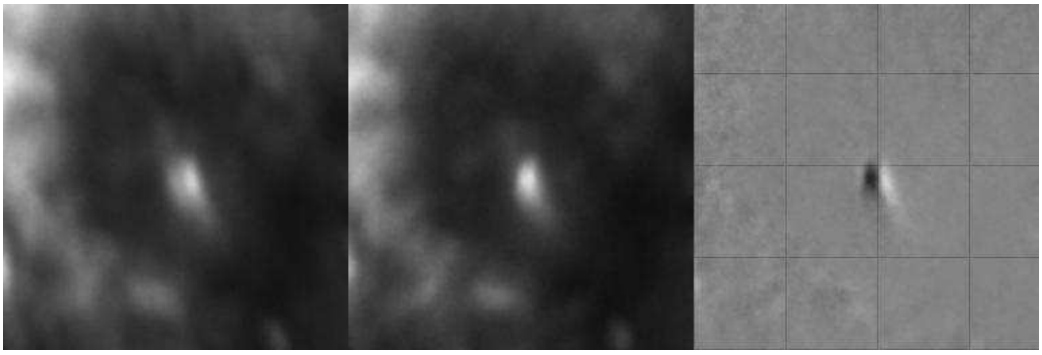

Figure 11: Detail of Feature 1. The three panels are I_+, I_0, and $I_+ - I_0$. The third panel has a 20″grid. From exposure 9 of 27, ∼18:45:41 UT, 3 s duration.

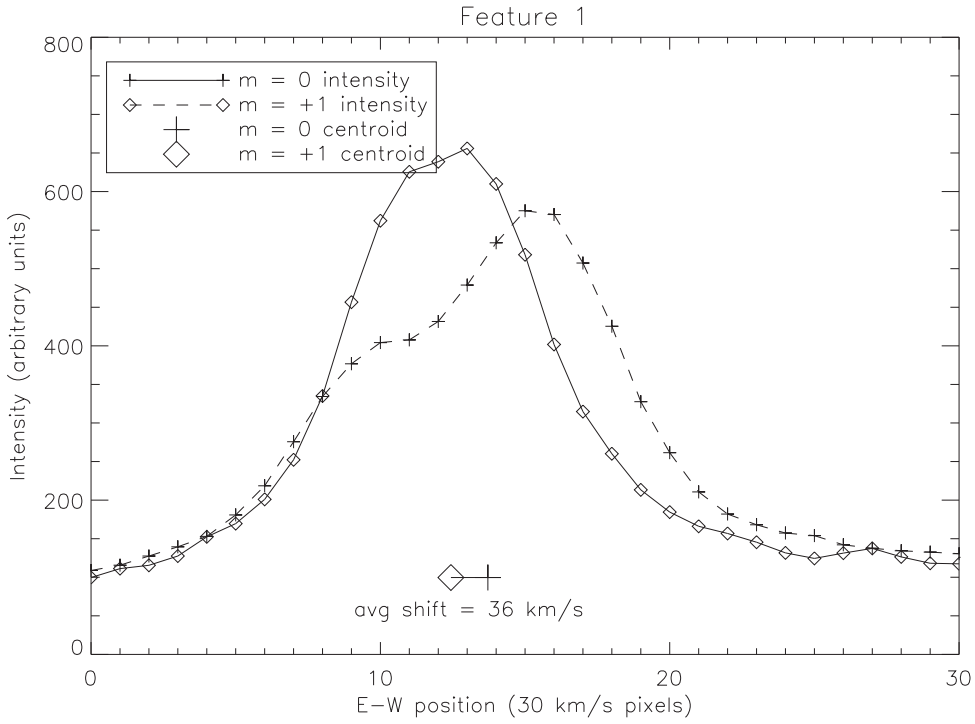

Figure 12: Intensity profiles along an east-west line through the core of Feature 1. From exposure 9, ∼18:45:41 UT, 3 s.

Feature 2 (figure 13) shows the strongest doppler shift found so far in the data set. The feature bifurcates into two bright kernels, both redshifted. The stronger redshift is 89 km/s, clearly supersonic for transition region temperatures (figure 14).

Feature 3 begins with a line broadening (figure 15) characteristic of a transition region explosive event. The northern end of a filament, seen in absorption, lies just to the west. Approximately one minute after the peak of the line broadening event, jets are seen shooting north and south from the bright kernel, parallel to the filament (figure 18). The bidirectional jets are offset, not from a common origin. The velocity estimations (figures 17 and 18) are both taken from the same exposure as figure 16. In figure 17, the broad line profile of the bright core is evident. The average velocity is essentially zero, but there appear to be two components: a bright peak with a weak blue shift and a dim peak with a strong red shift. Figure 18 shows the velocity estimate, -21 km/s, for the blue shifted (northern) jet.

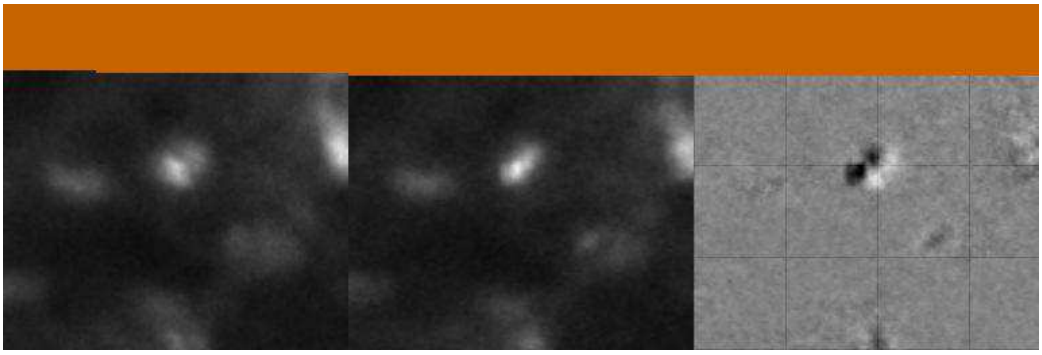

Figure 13: Detail of Feature 2. The three panels are I_+, I_0, and $I_+ - I_0$. From exposure 26, ∼18:49:07 UT, 0.75 s. The band at top is off the edge of the detector.

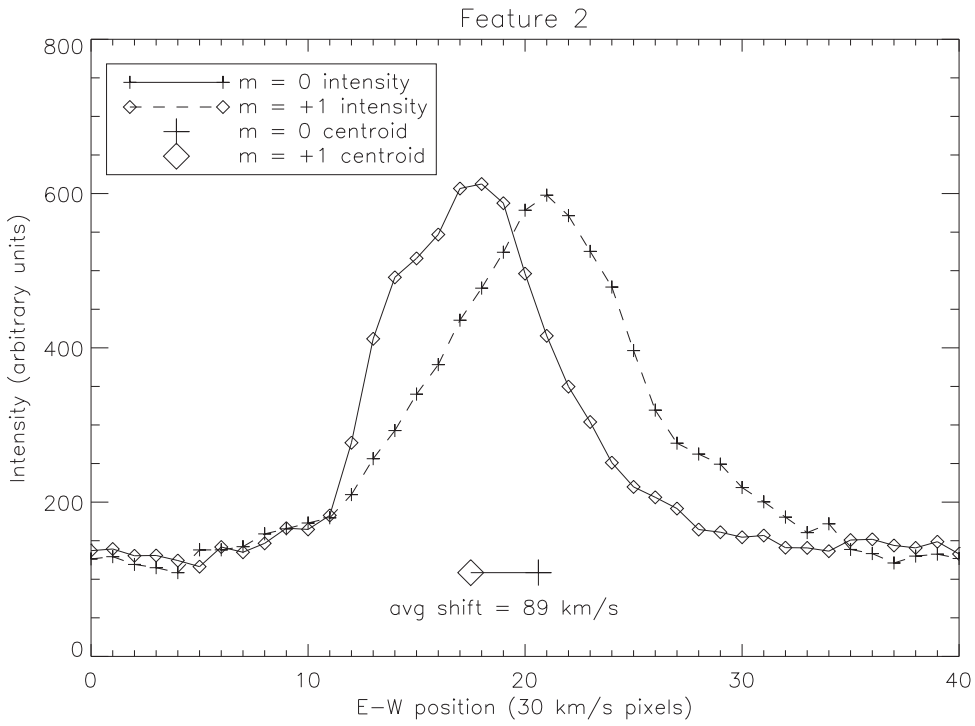

Figure 14: Intensity profiles along an east-west line through the strongest velocity signal in Feature 2. From exposure 26, ∼18:49:07 UT, 0.75 s.

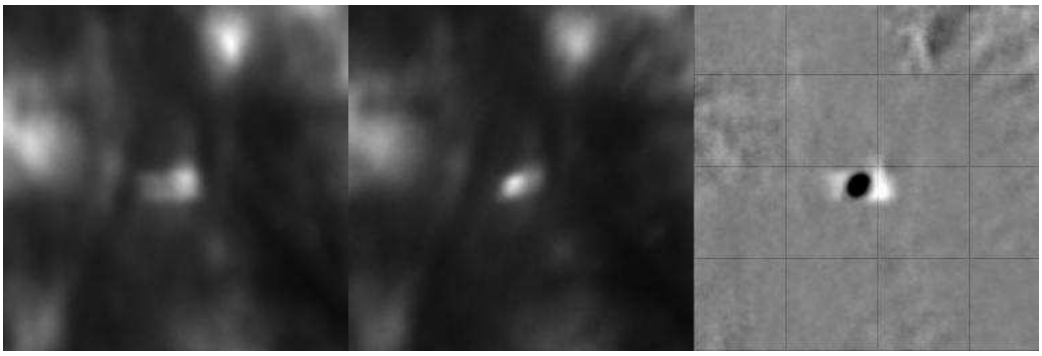

Figure 15: Detail of Feature 3. The three panels are I_+, I_0, and $I_+ - I_0$. From exposure 20, ∼18:47:42 UT, 3 s.

Figure 16: Detail of Feature 3. The three panels are I_+, I_0, and $I_+ - I_0$. From exposure 24, ∼18:48:52 UT, 6 s.

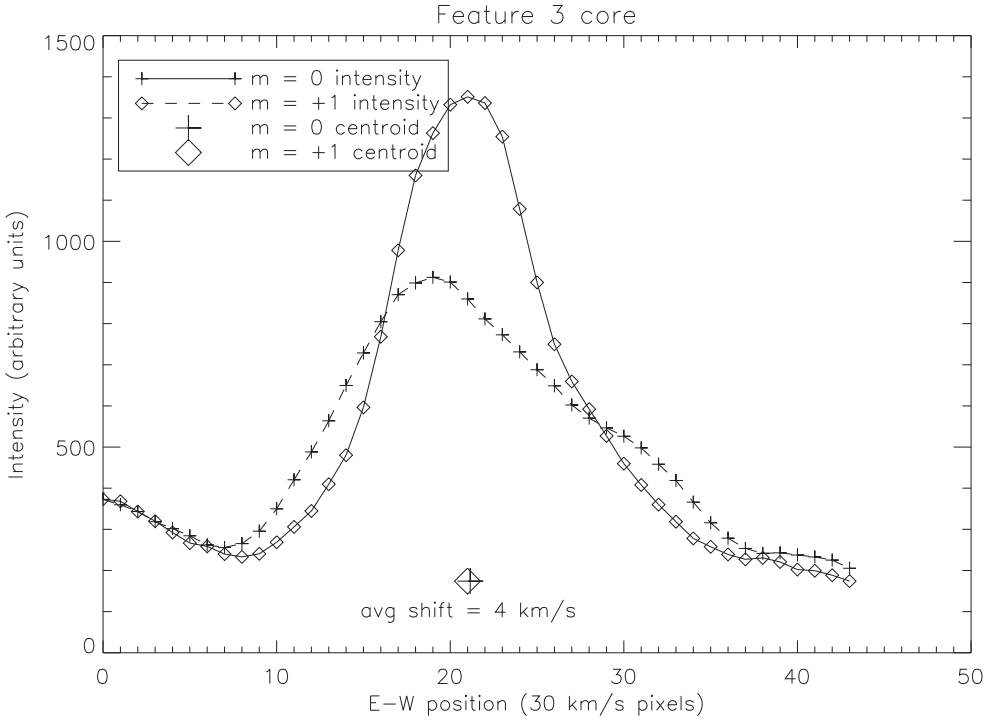

Figure 17: Intensity profiles along an east-west line through the bright core of Feature 3. From exposure 24, ∼18:48:52 UT, 6 s.

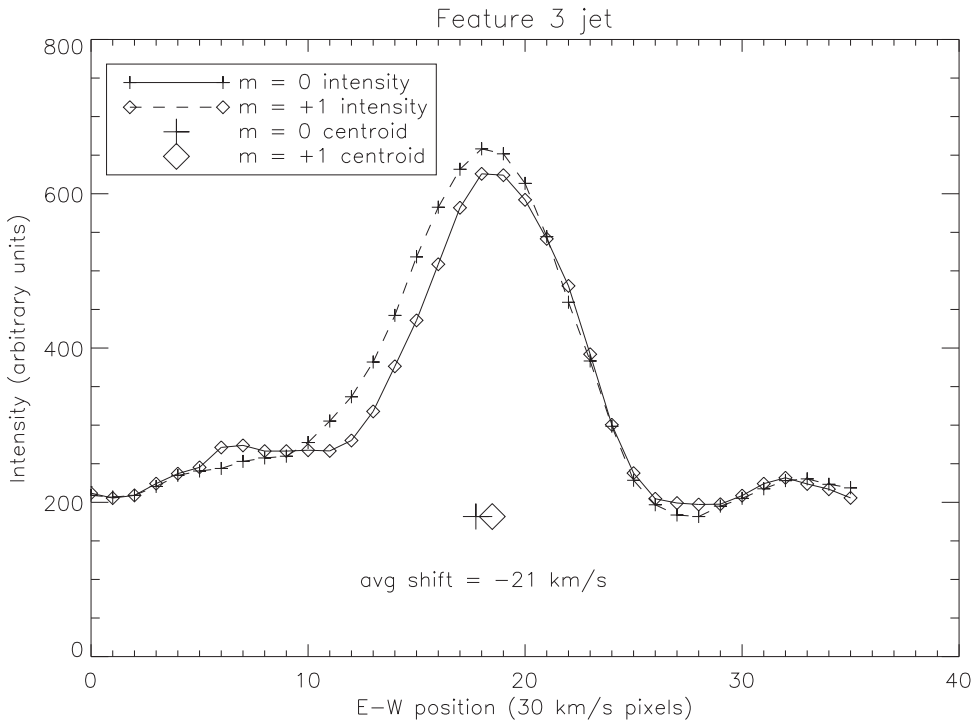

Figure 18: Intensity profiles along an east-west line through the upper (northern) jet of Feature 3, showing a blueshift. From exposure 24, ∼18:48:52 UT, 6 s.

7.2 Inversion techniques

Much can be gained from *MOSES* data using simple analysis techniques like those demonstrated in section 7.1. A step beyond this is inversion to obtain spectral information in every pixel.

The inversion of *MOSES* data is equivalent to tomography because each spectral order is a projection through position-and-wavelengh space (figure 19). The data are sparse, with only a few projections. Yet, the object $v(x, \lambda)$ itself is sparse because it contains mainly zeroes and a few spectral lines. In rough terms, the inversion works if there are as many projections as there are free parameters in the spectrum.

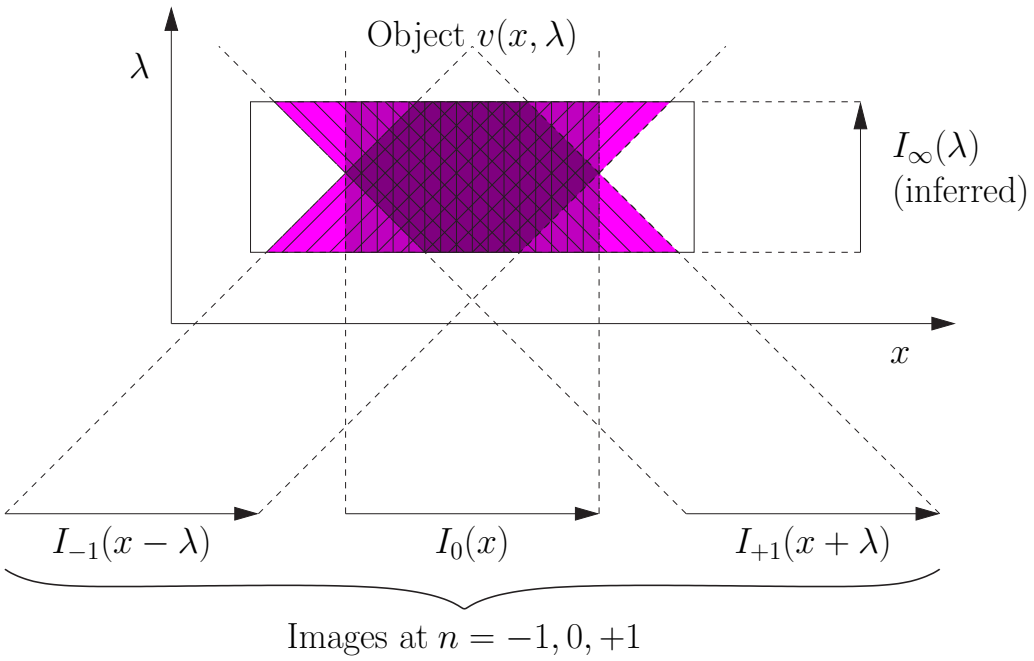

Figure 19: A visualization of the equivalence of *MOSES* data inversion to tomography. Three spectral orders are shown. There are only a small number of projections, so the data set is sparse.

A variety of inversion algorithms have been explored using test data. The key results are that (1) all the inversion techniques systematically underestimate the doppler shifts, but (2) even with no compensation for systematic error, the reconstructions allow doppler shifts to be determined with sub-pixel

(0.2-0.5 pixel RMS) accuracy (Fox, Kankelborg, & Metcalf 2003). Test data have included generated test patterns, SERTS spectrograms, and SUMER data cubes. The test algorithms include Fourier backprojection (iterated for positivity), a Pixon algorithm, and Smooth Multiplicative Algebraic Reconstruction Technique (SMART). The first two algorithms are reported in Fox & Kankelborg. The rest of the section will discuss the Fourier technique, its relation to singular value decomposition (SVD), and the SMART algorithm.

7.2.1 Fourier inversion and SVD

The Fourier Slice theorem (e.g. Kak & Slaney 1999) gives a direct pseudoinverse for equations 4 and 5. The Fourier transform of each of our projections corresponds with a slice through the origin of the Fourier transform of the object $v(x, \lambda)$:

$$\begin{aligned} \tilde{I}_m(k_x) &= \tilde{v}(u, mu), \\ \tilde{I}_\infty(k_\lambda) &= \tilde{v}(0, k_x). \end{aligned} \tag{3}$$

The wedges in between these slices of 2D Fourier space are undetermined, and therefore constitute the null space—the set of objects in $x\lambda$-space that produce a zero signature in all projections (§ A.2). The pseoudoinverse is implemented by zeroing the null space elements and using the Fourier-transformed data directly to fill the slices in $\tilde{v}$. It is no coincidence that this sounds much like SVD. The slices overlap slightly near the origin (or only at the origin, if there are just 3 orders like *MOSES*). If this overlap region is treated so that the result fits the data in a least-squares sense, then the Fourier pseudoinverse is identical to the SVD pseudoinverse.

The above reasoning (as well as the logic of projection) implies that null space elements have no DC component. They are oscillatory in nature, with a zero average along each of the measured (or inferred) projections (§ A.2). Kankelborg & Thomas (2001) derive the same properties of the null space by a different approach, expressing it interms of a compact, oscillating kernel function $\kappa(x, \lambda)$. Even crude knowledge of I_∞ constrains $v(x, \lambda)$ to be zero or very small over most of its domain; this combined with the positivity requirement leaves little room for the null space to operate, because the negative parts of any null space element must fall within the spectral line profile and be small enough in magnitude to avoid negatives. Since we expect line profiles to be smooth on the scale of the thermal width, a local smoothness constraint in the λ-direction can further reduce the ambiguity.

By itself, the pseudoinverse leads to unphysical solutions: they show a cross-hatched ringing pattern with many negative intensities. In the Fourier inversion method developed by Kankelborg (2002) (also Kankelborg & Fox 2003; Fox, Kankelborg, & Metcalf 2003), a trial solution is iteratively made nonnegative in real space, while the relevant slices in Fourier space are corrected to fit the data using equations 3. The null space wedges become filled in such a way as to make the solution positive. Local smoothness is intrinsic to this procedure.

7.2.2 SMART inversion

SMART (Smooth Multiplicative Algebraic Reconstruction Technique, Kankelborg & Fox 2004) is related to long-established algebraic reconstruction techniques (ART) developed for computed tomography (Kak & Slaney 1999). SMART differs from ART in that it begins with a positive initial guess and refines the fit to all spectral orders iteratively by multiplicative intensity adjustments. Positivity is thus inherent in the algorithm. Variable smoothing is introduced at each iteration, with the goal of convergence at $\chi^2_R = 1$. SMART is much faster than any of the techniques we have described previously, though the results from all these algorithms are similar. Results with a SUMER data cube have shown good separation of a weak coronal spectral line (near the noise floor, in fact) from a strong transition region spectral line (figure 20). The same reconstruction shows 0.2 pixel RMS accuracy in doppler shift reconstruction for the strong TR line (figure 21). In this example, velocities are computed only where there are 150 or more counts per pixel. The largest doppler shifts are about 1.5 pixels.

Figure 20: Reconstruction of integrated line intensities from a SUMER data cube by the SMART algorithm.

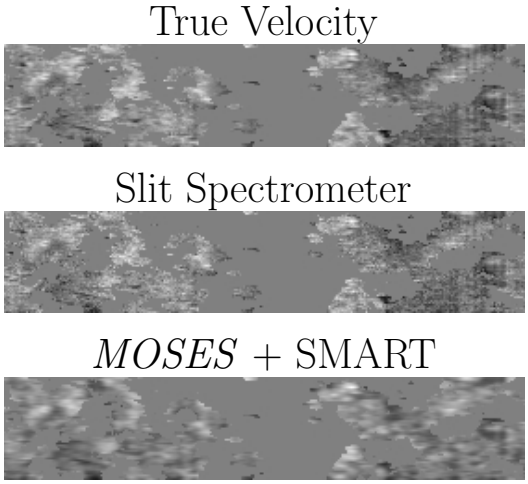

Figure 21: Estimation of doppler shifts from a SUMER data cube by the SMART algorithm. The middle panel shows the result of doppler shift estimation using slit spectrometer data with the same signal-to-noise ratio.

8 Conclusions

A new concept in high resolution imaging spectroscopy has been explored, and its usefulness has been demonstrated for observing the solar atmosphere in EUV. *MOSES* obtains narrowband images at rapid cadence like *TRACE* (Schrijver et al. 1999), but provides enough spectral information to measure doppler shifts anywhere within the field of view. Data from the first rocket flight have already yielded uniquely comprehensive data on transition region downflows and an explosive event.

Much more will be learned from the *MOSES* data when we invert to obtain spectra. We have elaborated a theory of the instrument, developed several inversion algorithms and completed successful inversions of simulated data. Before inversion algorithms can be applied to the rocket data, we must deduce the exact nature of the differences in PSF among the three spectral orders, and develop analysis techniques to compensate for these differences in the inversion. Solving this problem is the next goal of our analysis plan.

Though not discussed in the body of this report, we see evidence of the Si XI λ303.3 Å line when we compare the *MOSES* difference images with EIT 171 Å data. This evidence, and our prior simulation experience, suggest that

spectral inversions will yield a usable Si XI coronal image.

The *MOSES* rocket payload demonstrates the feasibility of a class of instruments with new observational capabilities. It is hoped that this development will find fruitful application in future space science missions (Kankelborg, Martens, & Thomas 2001; Martens & Kankelborg 2001; Harra et al. 2004; DeForest et al. 2004).

Acknowledgments

The success of *MOSES* owes much to collaborators around the world. Roger Thomas and collaborators at GSFC provided optical design, optical testing, multilayer coatings, and extensive support of calibration efforts. Mullard Space Science Laboratory (MSSL), with funding from PPARC, contributed a 3-CCD version of the EIS camera. The MSSL team provided invaluable assistance at solving interface issues and supporting our use of the camera. Marilyn Bruner influenced the optomechanical design and provided many words of wisdom. Her optical table system, developed for *SPDE*, flew on *MOSES* thanks to the cooperation of Lockheed-Martin Solar and Astrophysics Laboratory (LMSAL). The CDS program, Richard Harrison, Barry Kent and colleagues at Rutherford Appleton Laboratory invested many euros and hours in supporting our end-to-end calibration. Mission Manager Bill Payne, NSROC electrical engineers Jim Diehl and John Aasen, and the SPARCS team at WSMR provided unstinting, highly professional support of the mission from concept through launch.

The development and launch of *MOSES* was supported by the NASA Solar & Heliospheric Low Cost Access to Space program, grant NAG5-10997. Additional funding to support MSU students involved in *MOSES* was provided by the MSU Undergraduate Scholars Program, which is in turn supported by the Montana Space Grant Consortium. Lewis Fox has been supported for three years through a NASA GSRP award.

APPENDIX

A Theory

Here we present the theory behind *MOSES* measurements of spectral line profiles. The equations are cast in a form that allows consideration of a system with any number of spectral orders. The treatment is readily generalizable to include dispersion in the vertical as well has horizontal directions. An object $v(x, \lambda)$ forms images at spectral orders m:

$$I_m(x') = \int_B v(x' - m\lambda, \lambda)\, d\lambda, \tag{4}$$

where x' is the detector coordinate and domain B represents the passband of the instrument. For the *MOSES* rocket experiment, $m = (-1, 0, 1)$.[2] For convenience, position x' on the detector, position x on the Sun, and wavelength λ are all measured in pixels. The kernel is a projection operator. For example, in the $m = 1$ order, the above equation has $x = x' - \lambda$. A pixel at position x' receives light integrated along a slice $x + \lambda = x'$ in the $x\lambda$-plane (compare figure 19).

It is also helpful to define an "infinite" spectral order as follows:

$$I_\infty(\lambda) = \int_F v(x, \lambda)\, dx, \tag{5}$$

where F is the instrument field of view. This projection is of considerable interest, and will be taken up in § A.1. Once the spectral orders are intercalibrated, then the projections of $v(x, \lambda)$ obey a normalization condition,

$$N = \int_F I_m\, dx = \int_B I_\infty\, d\lambda = \int_B \int_F v\, dx\, d\lambda \tag{6}$$

for all orders m. The normalization condition holds exactly if the field of view is defined by a field stop prior to the dispersive element. Otherwise, the projections of the three orders will cover slightly different domains in (x, λ) at the edges of the field of view.

[2] We find this formulation more natural than the notation developed previously in Kankelborg & Thomas (2001)

A.1 Inferring the integrated spectrum

The average spectrum $I_\infty(\lambda)$ is not measured (though it could be, in principle). We infer it by a combination of prior knowledge and reasonable assumptions. The projection along the x-axis is special because it reveals the sparseness of the spectrum; that is, $v(x, \lambda)$ is mostly zeroes punctuated by a few spectral lines. For this reason, even a poor estimate of I_∞ greatly improves the inversion of equations 4 and 5 (Fox, Kankelborg, & Metcalf 2003).

The properties of the average spectrum, I_∞, may be well known due to prior observation; for example, previous observations indicate that the two spectral lines contained in the *MOSES* passband typically have a Gaussian profile (Andretta et al. 2000). It is also possible to find the position of a strong line and estimate its average line profile solely from the data. If we assume (only as a first guess) that the image and spectrum are separable,

$$v(x, \lambda) \sim \frac{1}{N} I_0(x)\, I_\infty(\lambda), \tag{7}$$

then the images at the dispersed spectral orders can be written in terms of the image at $m = 0$:

$$I_m(x) = \int_B \frac{1}{N} I_0(x - m\lambda)\, I_\infty(\lambda)\, d\lambda. \tag{8}$$

Using the convolution theorem, this leads immediately to an independent estimate of the fourier transform of the integrated spectrum for each $m \neq 0$. For example,

$$\tilde{I}_\infty = N \frac{\tilde{I}_{+1}}{\tilde{I}_0} = N \frac{\tilde{I}^*_{-1}}{\tilde{I}_0}. \tag{9}$$

Equation 7 assumes that the spectrum varies only in intensity. While this is not expected to be the case, we do expect these solutions to approximate the average spectrum. This approach may be tested quantitatively in at least two ways: (1) from simulation, using data from slit spectrometers like *SOHO*/SUMER; and (2) from real *MOSES* data by comparing the two independent solutions obtained from I_{-1} and I_{+1}. Our numerical experiments to date indicate that the profile of the strongest line can be obtained in this way.

A.2 Null space

The inversion of the integral equations 4 and 5 for $v(x, \lambda)$ is mathematically ill-posed. In principle, the three projections obtained by *MOSES* (four including I_∞) may be expected to contain less information than the original object (four functions of one variable compared to a function of two variables). However, prior knowledge about the spectrum, including its sparseness, smoothness and positivity, makes the problem tractable in practice. An understanding of the null space of the equations will clarify this point.

The null space is the set of possible variations of the object $v(x, \lambda)$ that lead to identical measurements. § 7.2.1 points out that the null space corresponds to a set of definite locations in the Fourier transform plane k_x, k_λ. Kankelborg & Thomas 2001 have derived the null space in the coordinate basis, and the following presentation follows their derivation. Treating I_∞ as just one of the projections I_m, we express our integral equations in terms of a linear operator T_m:

$$I_m = T_m \, v(x, \lambda). \tag{10}$$

If some other interpretation v' leads to the same data I_m, then

$$I_m = T_m \, v'(x, \lambda) \quad \Rightarrow \quad T_m \, (v' - v) = 0. \tag{11}$$

The null space is the set of functions $\mathcal{N}(x, \lambda)$ satisfying

$$T_m \, \mathcal{N} = 0 \quad \forall m. \tag{12}$$

Any such null space element can be written

$$\mathcal{N}(x, \lambda) = \int_F dx' \int_B d\lambda' \, \kappa(x - x', \lambda - \lambda') \, g(x, \lambda). \tag{13}$$

The function g must be zero at the boundaries of B. If a field stop is used, then g must also be zero at the boundaries of the FOV, F. The kernel of equation 13 is a differential operator,

$$\kappa(x, \lambda) = \left[\prod_m \hat{e}_m \cdot \nabla \right] \delta(x) \, \delta(\lambda), \tag{14}$$

$$\hat{e}_m = \frac{m\hat{x}}{\sqrt{1 + m^2}} - \frac{\hat{\lambda}}{\sqrt{1 + m^2}}. \tag{15}$$

The operator $\hat{e}_m \cdot \nabla$ is a partial derivative along the projection axis for order m. For example,

$$\hat{e}_0 \cdot \nabla = -\frac{\partial}{\partial \lambda}, \quad \hat{e}_{\pm 1} \cdot \nabla = \frac{1}{\sqrt{2}} \left(\pm \frac{\partial}{\partial x} - \frac{\partial}{\partial \lambda} \right), \quad \hat{e}_\infty \cdot \nabla = \frac{\partial}{\partial x}.$$

Since the detectors are pixellated, it is appropriate to construct κ in discrete space. For the *MOSES* rocket instrument, it takes the form:

$$\kappa = \begin{pmatrix} 0 & +1 & -1 & 0 \\ -1 & 0 & 0 & +1 \\ +1 & 0 & 0 & -1 \\ 0 & -1 & +1 & 0 \end{pmatrix}. \tag{16}$$

This is the smallest array of pixels having the property that the sum along any row, column or diagonal is zero; hence, the projection is zero for all $3+1$ spectral orders. Any null in a pixellated $x\lambda$-space must be a superposition of such patterns, as expressed by equation 13.

The above considerations are pivotal to solving the inverse problem. Successful inversion schemes use an estimate for I_∞ because it enforces the sparseness that is inherent to real, physical line spectra. Since the null functions have equal positive and negative flux, the positiviy requirement is very powerful. Null functions that yield positive solutions consist of oscillations which, because of I_∞, are confined within the envelope of the line profile(s) and thus have a small period in the λ direction. These remaining nulls are suppressed in our inversion schemes by assuming local smoothness of the solution. This may seem arbitrary, but it is an application of Occam's razor: the simplest solution is *a priori* most likely. Moreover, oscillations in λ smaller than the thermal width of the spectral line are not physically plausible.

Noise has not been considered in this discussion. Of course noise is inherent to the measurement process. Many inverse problems (such as image deblurring and differential emission measure) have kernels with smoothing properties that lead to high noise susceptibility. The kernel of equations 4 and 5 is a projection operator and therefore does not have this undesirable property. Our trial inversions have confirmed that even direct (Fourier) inversions of *MOSES* data do not amplify the noise in the data.

B Education

The *MOSES* mission has had far reaching educational impacts. Most of the payload, including optomechanics, custom circuits and software, was designed and built by undergraduate students under the mentorship of the PI and his graduate student. More than 30 students contributed meaningfully to this work. Many of these students have graduated and taken high tech jobs, including one working at LMSAL as a mechanical engineer on *STEREO*/SECCHI.

Graduate student J. Lewis Fox will base his dissertation on *MOSES*. Mr. Fox joined the project shortly after its inception in 2001. He led the team that developed the instrument electronics, did most of the system engineering, wrote the interface specifications for the payload, performed EUV calibration experiments at GSFC and RAL, and did most of the instrument operations during flight. He has developed and tested algorithms for data inversion (Fox & Kankelborg 2002; Fox, Kankelborg, & Metcalf 2003), and started modeling transition region turbulence (Fox & Kankelborg 2003) that might explain observed linewidths and intensities.

References

Andretta, V., Jordan, S. D., Brosius, J. W., Davila, J. M., Thomas, R. J., Behring, W. E., Thompson, W. T., & Garcia, A. 2000, ApJ, 535, 438

DeForest, C., Elmore, D. F., Bradford, M. P., Elrod, J., & Gilliam, D. L. 2004, ApJ, 616, 600

Fox, J. L., & Kankelborg, C. C. 2002, American Astronomical Society Meeting, 200

Fox, J. L., & Kankelborg, C. C. 2003, American Astronomical Society Meeting

Fox, J. L., Kankelborg, C. C., & Metcalf, T. R. 2003, in Optical Spectroscopic Techniques and Instrumentation for Atmospheric and Space Research V. Edited by Larar, Allen M.; Shaw, Joseph A.; Sun, Zhaobo. Proceedings of the SPIE, Volume 5157, pp. 124-132 (2003)., ed. A. M. Larar, J. A. Shaw, & Z. Sun, 124

Harra, L., Kankelborg, C., Thomas, R., Fox, J., & Winter, B. 2004, in 35th COSPAR Scientific Assembly, 1120

Kak, A. C., & Slaney, M. 1999, Principles of computerrized tomographic imaging (IEEE Press)

Kankelborg, C. C. 2002, American Astronomical Society Meeting, 200

Kankelborg, C. C., & Fox, J. L. 2003, American Astronomical Society Meeting

Kankelborg, C. C., & Fox, J. L. 2004, American Astronomical Society Meeting Abstracts, 204, 69.01

Kankelborg, C. C., Longcope, D. W., & Martens, P. C. H. 2000, AAS/Solar Physics Division Meeting, 32

Kankelborg, C. C., Martens, P. C., & Thomas, R. J. 2001, in Solar Encounter: Proc. 1st Solar Orbiter Workshop, 257

Kankelborg, C. C., & Thomas, R. J. 2001, in Proc. SPIE Vol. 4498, UV/EUV and Visible Space Instrumentation for Astronomy and Solar Physics, ed. O. H. Siegmund, S. Fineschi, & M. A. Gummin, 16

Martens, P. C., & Kankelborg, C. C. 2001, in Solar Encounter: Proc. 1st Solar Orbiter Workshop, 293

Nowak, M. 2004, private communication

Owens, S. M., et al. 2005, in Optics for EUV, X-Ray, and Gamma-Ray Astronomy II. Edited by Citterio, Oberto; O'Dell, Stephen L. Proceedings of the SPIE, Volume 5900, pp. 5-13 (2005)., ed. O. Citterio & S. L. O'Dell, 5

Schrijver, C. J., et al. 1999, Sol. Phys., 187, 261

Thomas, R. J. 2006, private communication

Thomas, R. J., & Kankelborg, C. C. 2001, American Astronomical Society Meeting, 199